Behavior of helium cavities in ion-irradiated W-Ni-Fe ductile-phase toughened tungsten

Weilin Jiang [a,*], Dalong Zhang [a], Dongsheng Li [a], Jaeyoung Heo [a], Zhiqiang Wang [b], Limin Zhang [b], Nicole Overman [a], Tamas Varga [a], Zhihan Hu [c], Xuemei Wang [c], Lin Shao [c], Wahyu Setyawan [a]

[a] *Pacific Northwest National Laboratory, Richland, WA, United States*
[b] *School of Nuclear Science and Technology, Lanzhou University, Lanzhou, Gansu, PR China*
[c] *Department of Nuclear Engineering, Texas A&M University, College Station, TX, United States*

HIGHLIGHTS

- The diameter of He cavities in NiFeW is ~5 times larger than in W.
- The number density of He cavities in NiFeW is ~2 orders of magnitude lower than in W.
- Preferential formation of He cavities is observed along the NiFeW/W interphase boundary.
- There is a uniform distribution of He cavities across the W grain boundary.
- Pre-irradiation with Ni^+ ions could create trapping centers for migrating vacancies and He atoms.
- Formation of He cavities is attributed to diffusion, clustering and trapping of vacancies and He atoms.

ABSTRACT

This study reports on the distribution of helium (He) cavities in a hot-rolled W-Ni-Fe ductile-phase toughened tungsten (DPT W) composite irradiated to a dose and a helium concentration that are comparable to those in the material after 5-year irradiation in a conceptual fusion power plant. The DPT W sample consists of W particles embedded in a ductile-phase NiFeW matrix with a nominal composition of 90W-7Ni-3Fe by weight. It was hot-rolled to a thickness reduction by 87% (87R DPT W). Sequential and individual irradiations of the material with 1.2 MeV Ni^+ ions to a fluence of 2.15×10^{16} Ni^+/cm^2 and 90 keV He^+ ions to 6.5×10^{15} He^+/cm^2 was performed at 973 K. Larger He cavities with a lower number density are observed in NiFeW than W. Helium cavities are aggregated preferentially along the NiFeW/W interphase boundary. This behavior is not observed along the W/W grain boundary under the same irradiation conditions. The average corrected cavity diameter or volume appears to be smaller in the sequentially irradiated sample than He^+ ion irradiated sample. There is no evidence for formation of visible voids or Ni precipitates in W phase irradiated with Ni^+ ions only. Diffusion, clustering and trapping of vacancies and He atoms during He^+ ion irradiation at 973 K may be responsible for the formation of the He cavities.

Keywords: Helium cavity, ion irradiation, ductile-phase toughened tungsten

[*] Corresponding author. *E-mail address:* weilin.jiang@pnnl.gov (W. Jiang).

1. Introduction

Tungsten (W) possesses various favored properties for use as plasma-facing materials in fusion power systems, including high melting point (3695 K), good thermal conductivity (175 W/(m·K)), high resistance to material sputtering and chemical erosion, low swelling rate, low activation, and low tritium retention [1-6]. However, pure W has low fracture toughness and its ductile to brittle transition temperature (DBTT) increases with irradiation damage [7,8]. To address the issues, ductile-phase toughened tungsten (DPT W) composites, including W-Ni-Fe DPT W, have been explored [9-12]. The W-Ni-Fe DPT W composite consists of predominant brittle-phase W particles embedded in a small fraction of ductile-phase matrix of Ni-based NiFeW solid solution, thus being able to retain the major properties of W. The ductile phase can prevent or inhibit crack propagation by crack blunting, crack bridging, crack deflection, and crack branching [9]. The W particles in a DPT W plate rolled to 87% thickness reduction (87R DPT W) are elongated, flattened, and merged. The continuous nature of the NiFeW phase provides a ductile tearing path through this material, limiting crack progression at the heterogeneous interface. Ductile-phase toughening mechanism relies on a strong interfacial cohesion between the brittle W particle and ductile NiFeW matrix. A recent study [12] shows that microcracking at the interphase boundaries is predominantly blunted and arrested by the ductile phase with little to no instances of interfacial debonding.

Accumulation of He gas could potentially be detrimental to the W/NiFeW interfacial cohesion. It is important to study He cavity behavior in both phases as well as along the interphase boundaries. Due to a lack of 14 MeV neutron sources with a suitable flux, irradiation studies of fusion materials have been performed primarily using surrogates of fission reactor neutrons (up to 2 MeV) and accelerator-based ion beams. To our best knowledge, irradiation studies of any DPT W composites have not yet been reported to date. This study attempts to emulate and characterize the microstructure in DPT W irradiated at 973 K with self-ion (Ni^+) and He^+ ion beams to a dose and a helium concentration that are comparable to those in the material after 5-year irradiation in a conceptual fusion power plant.

2. Experimental details

A high-density DPT W composite, consisting of brittle W particles (88 wt.%) embedded in a ductile NiFeW matrix (12 wt.%) with 54.68 wt.% Ni, 22.57 wt.% Fe and 22.75 wt.% W, was fabricated by liquid-phase sintering of Mi-Tech Metals stock powders [13,14] at 1,773 K in a hydrogen environment; the material was subsequently hydrogen degassed at 1,273 K in vacuum [12]. The DPT W samples were rolled in a number of passes at 1,423 and 1,173 K to a final 87% thickness reduction, followed by hydrogen degassing at 1,173 K in vacuum [9]. Hot-rolling changes the spherical W particles to elongated plates and increases W-W connectivity. A surface-polished 87R DPT W sample (4 mm × 13 mm × 2 mm) was characterized prior to ion irradiation using a number of methods. Symmetric 2θ-ω XRD was performed using a Philips X'Pert multipurpose diffractometer (MPD) with a fixed Cu anode ($\lambda_{K\alpha}$ = 0.154 nm) operating at 45 kV and 40 mA. Whole pattern fitting (Rietvelt refinement) was performed to obtain the average crystallite size and weight percentage of the W and NiFeW phases using TOPAS-64 V6 software. The best data fit was achieved using ICDD database PDF 00-004-0806(RDB) for W (Im-3m, a = 0.31648 nm) and ICSD database 103558 for $FeNi_3$ (Fm-3m, a = 0.35556 nm) as the database did not contain any NiFeW phases. Both backscattered electron (BSE) imaging and energy dispersive spectroscopy (EDS) were also performed using a JEOL 7600 FESEM. To minimize the excitation volume for more accurate detection of the composition in relatively small volumes of W or NiFeW, a low

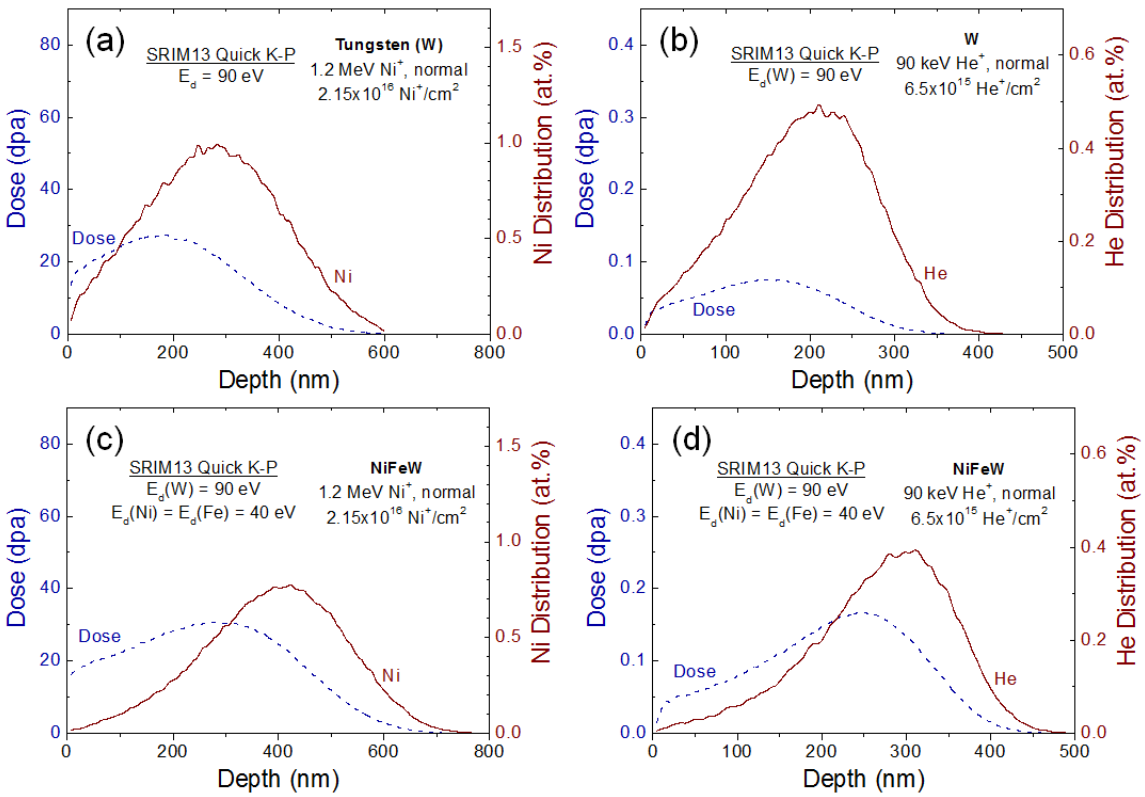

Figure 1. Depth profiles of doses and atomic percentages from quick K-P SRIM13 simulations for (a) 1.2 MeV Ni^+ irradiation of W to 2.15×10^{16} Ni^+/cm^2, (b) 90 keV He^+ irradiation of W to 6.5×10^{15} He^+/cm^2, (c) 1.2 MeV Ni^+ irradiation of NiFeW to 2.15×10^{16} Ni^+/cm^2, and (d) 90 keV He^+ irradiation of NiFeW to 6.5×10^{15} He^+/cm^2.

accelerating voltage (5 kV) for the primary electrons was selected. In addition, electron backscatter diffraction (EBSD) was performed using a JEOL 7001F FESEM at an operating voltage of 20 kV. The EBSD data was collected at a tilting angle of 70°. The scan was conducted over an area of 123 µm × 92 µm with a step size of 175 nm. Data analysis was accomplished using Oxford HKL Tango software. Structural parameters for bcc W (a = 0.31650 nm) and fcc $FeNi_3$ (a = 0.35560 nm) were chosen for phase indexing because there are no phase data reported for NiFeW alloys.

Based on model calculations of elemental transmutation and gas production, Gilbert *et al*. [15] have predicted the He production in the first wall of a conceptual fusion power plant at a total neutron flux of 1.04×10^{15} (n/cm^2)/s. Calculations [15] show that a He concentration of 1,090 appm is produced from Fe and 33.6 appm from W after 5-year irradiation in the fusion power plant. The He production from Ni (2,442 appm) is estimated based on that from Fe using the reaction cross sections of Ni (99.9 mb) and Fe (44.6 mb) with 14 MeV neutrons [16]. The total He concentration produced in NiFeW is 1,863 appm or ~0.19 at.%. The dose in displacements per atom (dpa) in W is estimated to be 27.4 dpa after 5-year irradiation in the fusion power plant based on the data reported in [17] after the neutron flux is adjusted to 1.04×10^{15} (n/cm^2)/s [15].

In order to emulate irradiation effects in DPT W by 14 MeV neutrons using ion irradiation, sequential irradiation of self-ion (Ni^+) and He^+ ions was applied. Because the factors of the maximum primary knock-on atom (PKA) energy for Fe or Ni ions are closer to the factor for neutrons than W ions, the lighter ions are a better choice for self-ion irradiation in terms of better emulation of damage cascades.

Table 1. Quick K-P SRIM13 simulation results for Ni^+ and He^+ ion irradiations in W and NiFeW.

Ion	Material	Damage Peak Depth (nm)	Peak Dose (dpa)	Ni or He Peak Depth (nm)	Ni or He Peak Concentration (at. %)
1.2 MeV Ni^+ 2.15×10^{16} Ni^+/cm^2	W	168	27	294	0.98
90 keV He^+ 6.5×10^{15} He^+/cm^2	W	160	0.074	215	0.48
1.2 MeV Ni^+ 2.15×10^{16} Ni^+/cm^2	NiFeW	296	31	416	0.76
90 keV He^+ 6.5×10^{15} He^+/cm^2	NiFeW	250	0.17	295	0.39

Note: NiFeW phase contains 63.83 at.% Ni, 27.69 at.% Fe and 8.48 at.% W

Because the PKA energy factors for Fe and Ni ions are comparable in value and Ni is the dominant element in the NiFeW phase, Ni ions are selected as self-ions to emulate high-energy neutron irradiation in this study. In addition, because He atoms would typically migrate in NiFeW phase with irradiation damage, sequential irradiation was performed first with Ni^+ and then He^+ ions with the He concentration maximum spatially overlapped with the Ni damage peak. In order to estimate dose rates and He distributions in W and NiFeW, SRIM13 (Stopping and Range of Ions in Matter, version 2013 [18]) simulations under the quick Kinchin-Pease (K-P) mode were carried out for 1.2 MeV Ni ions and 90 keV He ions in W and NiFeW, where the threshold displacement energies of $E_d(W)$ = 90 eV and $E_d(Ni)$ = $E_d(Fe)$ = 40 eV were adopted [19] and the lattice binding energy was set to 0 eV [20]. The density is assumed to be 19.25 g/cm^3 or 6.3×10^{22} at./cm^3 for body-centered cubic W and 9.50 g/cm^3 or 8.3×10^{22} at./cm^3 for face-centered cubic NiFeW. The simulation results for ion fluences of 2.15×10^{16} Ni^+/cm^2 and 6.5×10^{15} He^+/cm^2 in W and NiFeW are shown in Fig. 1 and summarized in Table 1. It should be noted that SRIM simulations do not involve any thermal diffusion of point defects and implanted species.

For Ni^+ ion irradiation in W, the peak dose is 27 dpa at 168 nm, comparable to the dose in W after 5-year irradiation in a conceptual fusion power plant [15,17] as described above; in NiFeW, the corresponding peak dose is 31 dpa at 296 nm. For He^+ ion irradiation in NiFeW, the maximum He concentration is 0.39 at.% at 295 nm. The He peak is well aligned with the Ni damage peak, as designed. This He concentration (0.39 at.%) is about a factor of 2 higher than the above estimated (0.19 at.%). It is chosen in this study because a significant amount (assumed to be ~50%) of the implanted He atoms is expected to release during He^+ ion irradiation at 973 K. It should be mentioned that quick K-P simulation adopted by this study predicts the vacancy production rates by only a small difference from 0 to 30% compared to a new approach [21] that uses the full-damage cascade option in SRIM13 with manual manipulation of irradiation parameters, in a sharp contrast to the rates obtained without parameter corrections that overestimate the values by a factor of 1.1 to 4. Under the irradiation conditions of this study, the average number of vacancies produced by one Ni^+ or He^+ ion in W or NiFeW from the full-cascade simulations without parameter corrections is ~2 times larger than that from the quick K-P simulations.

Sequential irradiation with 1.2 MeV Ni^+ and 90 keV He^+ ions was performed at 973 K using a 3.0 MV tandem ion accelerator and a 120 kV single-ended ion accelerator at the Texas A&M University, respectively. Fig. 2 shows a schematic sketch for the sequence of ion irradiation. An area of 4 mm × 7 mm was first irradiated to 2.15×10^{16} Ni^+/cm^2. Subsequently, an area of 4 mm × 8 mm was irradiated to 6.5×10^{15} He^+/cm^2 with an overlapping area of 4 mm × 4 mm, as shown in Fig. 2, thus creating 3 regions of irradiation with Ni^+ ions only, both Ni^+ and He^+ ions, and He^+ ions only. The average ion fluxes were 4.0×10^{12} $(Ni^+/cm^2)/s$ and 3.6×10^{12} $(He^+/cm^2)/s$. There was also an unirradiated area of 4 mm × 2 mm. A resistance heater was located behind the copper plate on which the sample was mounted. The temperature was monitored using a thermocouple on a copper plate. The irradiation was performed with a rastering system to achieve a uniform irradiation over the intended areas.

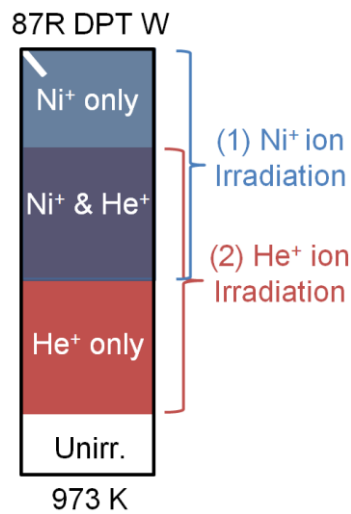

Figure 2. Schematic sketch of an 87R DPT W sample irradiated sequentially to first 2.15×10^{16} Ni^+/cm^2 and then 6.5×10^{15} He^+/cm^2 at 973 K to create three different irradiation regions and an unirradiated region.

Cross-sectional transmission electron microscopy (TEM) specimens of the irradiated 87R DPT W were prepared using a FEI Quanta dual-beam focused ion beam (FIB) microscope. Due to a significantly higher sputtering rate from NiFeW than W, additional thinning for W was performed. A few keV Ga^+ ion beam was used for final polishing of the FIB specimens. Fresnel under- and over-focus techniques were employed to observe cavities in the irradiated samples using a JEOL JEM-ARM 200CF aberration-corrected scanning TEM microscope (STEM) and a Tecnai F20 TEM microscope (Thermofisher, USA), both operating at 200 kV. The statistical analysis of the cavity diameters was performed manually, assisted by the DT2000 General Image Analysis Software, as described previously [22]. The inner diameter of the first dark Fresnel ring D_{in} is determined by a circle with diameter $D_{in} = \sqrt{4A_{in}/\pi}$, where A_{in} is the area of the circle. The actual cavity diameter D_0 was deduced from D_{in} using a correction factor from a simulation report [23]. The number density is determined by the cavity counts divided by the area and local foil thickness in the center of the area determined by electron energy loss spectroscopy (EELS).

3. Results and discussion

3.1. Characterization of as-polished 87R DPT W

Fig. 3 shows a typical BSE image for an 87R DPT W composite. The dark and brighter areas are NiFeW and W, respectively. The W phase is elongated and well interconnected due to hot-rolling process. Five areas from each of the phases (W1 – W5 and NiFeW1 – NiFeW5) were chosen for EDS analysis. The results from all the areas W1 – W5 are

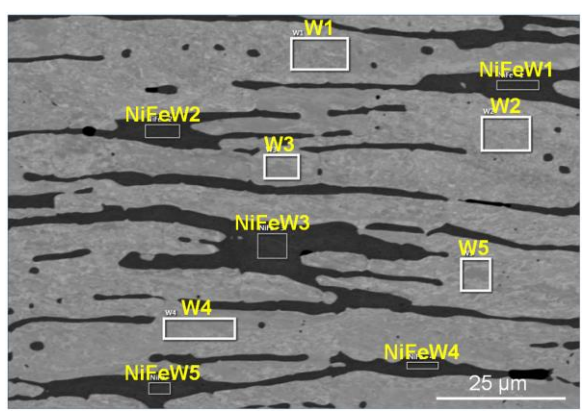

Figure 3. Plan-view BSE image for an as-polished 87R DPT W sample with the areas indicated for EDS measurements.

found to be 100% W within the detection limit. While the use of a low accelerating voltage (5 kV) for EDS can minimize the interference from the neighboring compositions, it reduces the detection sensitivity for Ni and Fe in W. Although 5 keV electrons cannot produce Fe K_α (6.4 keV) and Ni K_α (7.5 keV) X-rays, they can excite emission of Fe L_α (0.71 keV) and Ni L_α (0.85 keV) X-rays. However, the latter peaks are weak in intensity and are located in a high background region (data not shown). The peaks cannot be well resolved, but small percentages of Ni and Fe in W could be present, as detected by 200 keV STEM-EDS line scans (see Fig. 14). The weight percentages of each element in areas from NiFeW1 to NiFeW5 are determined by L_α X-ray peak intensities, as given in Table 2. The average values are 54.68 wt.% Ni, 22.57 wt.% Fe and 22.75 wt.% W with a standard deviation of less than 2 wt.%. It should be noted that trace oxygen (~1%) and carbon (~2%) were also present in the EDS spectra, but were removed as background contamination.

Table 2. Composition of the NiFeW phase in 87R DPT W from EDS.

Spectrum	Ni (wt. %)	Fe (wt. %)	W (wt. %)
NiFeW1	54.91	22.61	22.48
NiFeW2	55.83	23.46	20.71
NiFeW3	53.38	21.81	24.81
NiFeW4	55.92	22.91	21.18
NiFeW5	53.35	22.09	24.56
Average	54.68	22.57	22.75
Standard Deviation	1.26	0.66	1.89

Note: 87R DPT W contains 88 wt.% W and 12 wt.% NiFeW.

The EBSD pattern quality, phase map and grain orientation map of the as-polished 87R DPT W composite are shown in Fig. 4, where the black areas are the unindexed regions that include grain boundaries and lattice distortions (strain). The mottled features inside the grains shown in Fig. 4(a) may be attributed to the surface damage introduced either during polishing or rolling. The unindexed, W and NiFeW regions occupy 1.325%, 89.14% and 9.54% areas, respectively, as obtained from the phase map in Fig. 4(b). From Fig. 4(c), it is seen that the grain orientations in the out-of-plane (Z) view direction are randomly distributed without a preferred orientation. Some of the individual grains show a color contrast, suggesting that there may be some lattice stress in the grains.

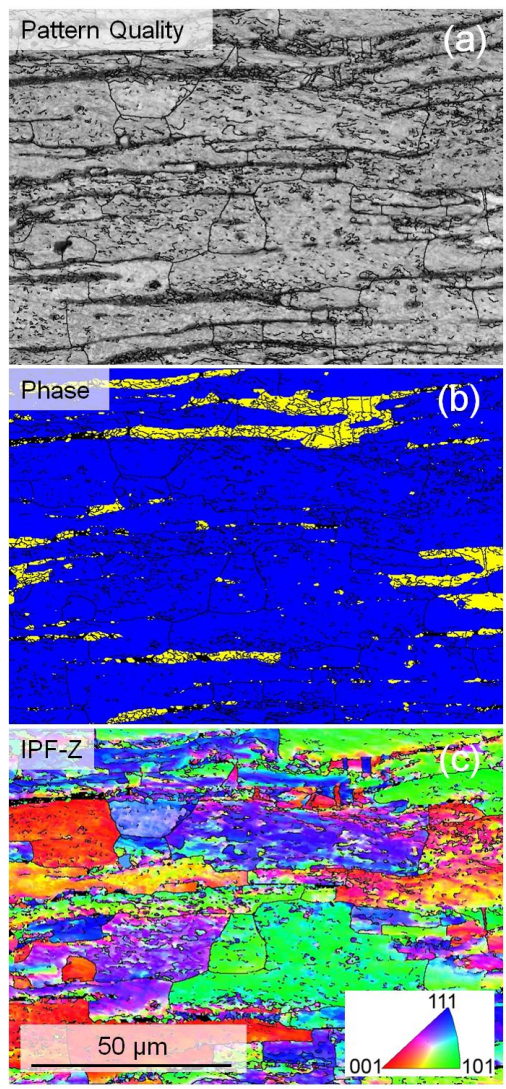

Figure 4. (a) EBSD pattern quality image, (b) phase map (blue for W, yellow for NiFeW) and (c) grain orientation map for an as-polished 87R DPT W sample.

Fig. 5 shows the X-ray diffraction pattern for the as-polished 87R DPT W sample. All the major diffraction peaks can be indexed, as indicated in the figure. $FeNi_3$ is used for indexing the NiFeW phase, as noted above. The whole-pattern data fit suggests that the average crystallite sizes for the W and NiFeW phases are 141 and 60 nm, respectively. The average crystallite size is the average inter-planar distance between the adjacent planar defects that discontinue the lattice periodicity in a crystalline grain. In principle, crystallite size should not be greater than a grain size. Typically, the smaller the average crystallite size, the higher the defect concentration in a crystalline grain. In addition, the data fit leads to weight percentages of 88 wt.% W and 12 wt.% NiFeW in the 87R DPT W composite. Considering the elemental weight percentages in the NiFeW phase (Table 2), the overall weight percentage in the composite is 90.8 wt.% W, 6.6 wt.% Ni and 2.6 wt.% Fe.

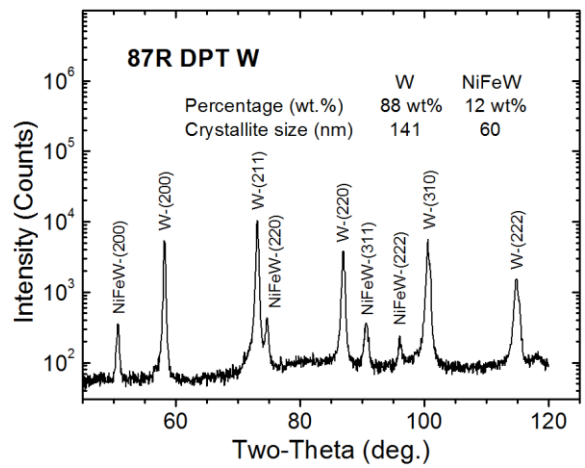

Figure 5. XRD pattern for an as-polished 87R DPT W sample. $FeNi_3$ phase was used to index the NiFeW phase.

3.2. Helium cavities in 87R DPT W irradiated sequentially with Ni^+ and He^+ ions

3.2.1. General features of the microstructure

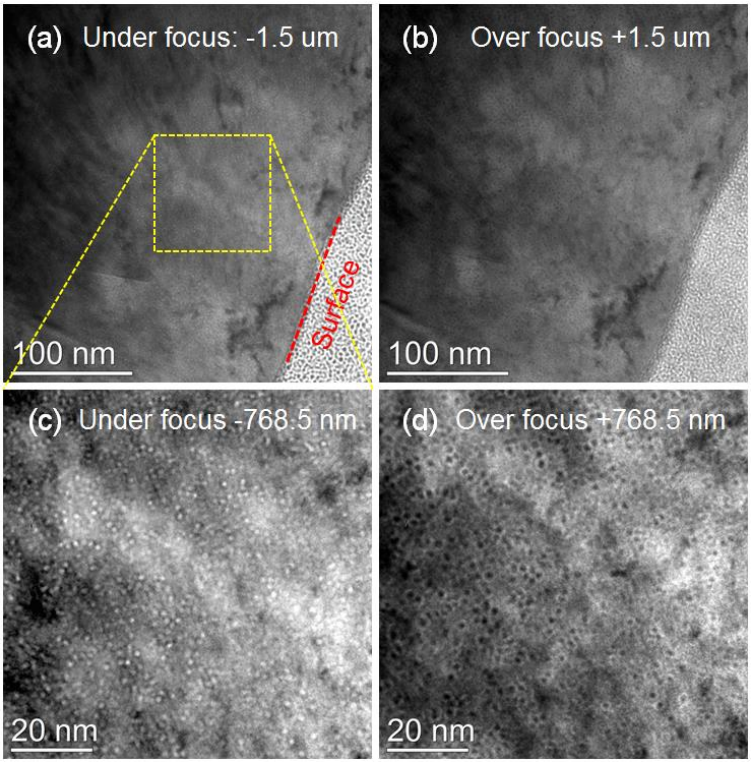

Figure 6. A low-magnification TEM view of the spatial distributions of He cavities in the W phase within an 87R DPT W sample irradiated sequentially to 2.15×10^{16} Ni^+/cm^2 and 6.5×10^{15} He^+/cm^2 at 973 K: (a) under focus and (b) over focus and a higher-magnification view at the image center depth of ~100 nm: (c) under focus and (d) over focus.

Fig. 6 shows a cross-sectional view of the microstructure in the near-surface region of a W grain within 87R DPT W irradiated sequentially to 2.15×10^{16} Ni^{+}/cm^{2} and 6.5×10^{15} He^{+}/cm^{2} at 973 K. There is a high density of small spots that change their contrast from bright in the under-focus image [Figs. 6(a) and (c)] to dark in the over-focus image [Figs. 6(b) and (d)], indicating that these features are cavity-type defects or He cavities from Fresnel diffraction. The size distribution of the cavities is relatively uniform over the depth region from 0 to 300 nm due to rapid diffusion of He atoms and mono-vacancies in W during He^{+} irradiation at 973 K. At depths larger than 300 nm from the surface, He cavities in W are hardly visible due to larger foil thickness and probably a lower cavity number density in W as well.

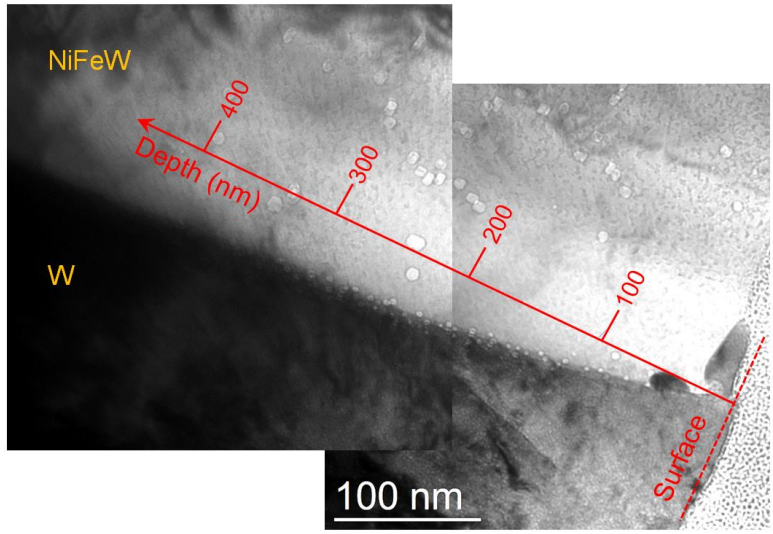

Figure 7. A general TEM view of the microstructure in the surface region of an 87R DPT W sample irradiated sequentially to 2.15×10^{16} Ni^{+}/cm^{2} and 6.5×10^{15} He^{+}/cm^{2} at 973 K.

A general view of the microstructure in the surface region of the sample is shown in Fig. 7. Besides in W, He cavities are also observed in NiFeW and along their interphase boundary. The cavities in NiFeW are distributed mainly in the depth region from 200 to 300 nm. Compared to other regions, the cavities in the NiFeW region are larger but their number density is lower. The different He cavity number densities and sizes in W and NiFeW phases reflect the efficiencies of nucleation and growth of He cavities in the two different materials, which may be generally associated with the production rates of mono-vacancies, He and vacancy diffusivities, and formation probabilities of stable He-vacancy clusters. The size of the He cavities along the W/NiFeW interphase boundary is between those in the two phases. The number density appears to be high, showing that the interphase boundary has a great strength of trapping vacancies and He atoms for aggregation of He cavities. In general, the cavity number density and cavity size depend on the defect mobility and trapping efficiency in the nucleation and growth processes. Further research, including modeling efforts, is needed to better understand the preferential formation of cavities along the interphase boundaries as well as the cavity size range, which is beyond the scope of this study.

3.2.2. Helium cavity distribution

Fig. 8(a) shows an under-focus TEM image for W irradiated with Ni^{+} and He^{+} ions. The image center is located at the depth of ~100 nm with the surface direction indicated in the figure. A high density of small He cavities is observed. Each cavity in the imaged area is counted and its diameter of the first dark Fresnel ring is measured. The average diameter of the first ring can be calculated using

$$D_{in} = \frac{1}{n}\sum_{i=1}^{n} D_{in}^{i}, \quad (1)$$

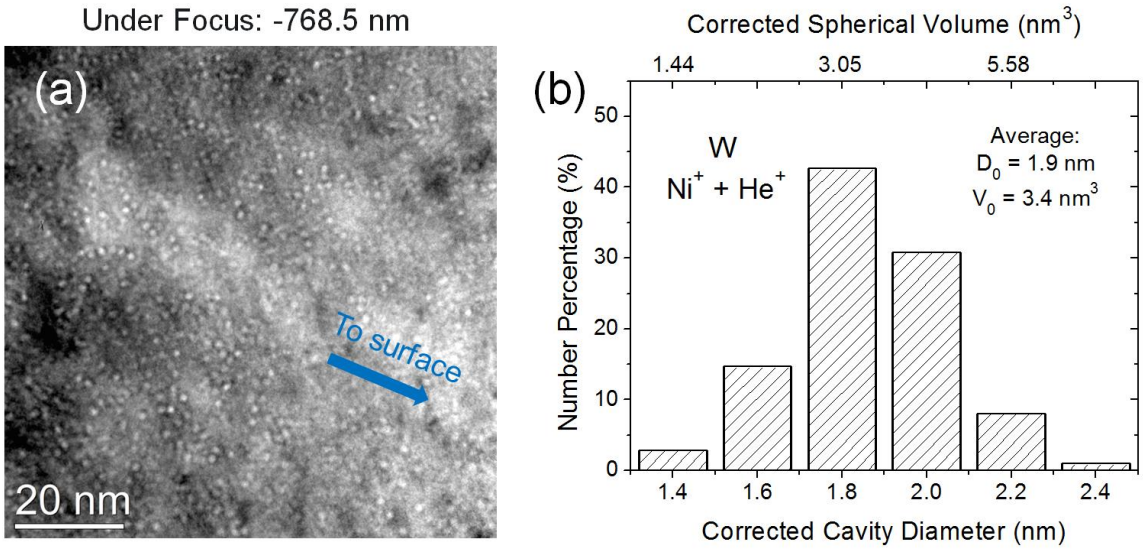

Figure 8. (a) TEM image showing a spatial distribution of He cavities at the image center depth of ~100 nm in the W phase within an 87R DPT W sample irradiated sequentially to 2.15×10^{16} Ni^+/cm^2 and 6.5×10^{15} He^+/cm^2 at 973 K. (b) Corrected He cavity diameter and volume distributions.

Table 3. Average inner diameter (D_{in}) of the first dark Fresnel ring, average corrected cavity diameter (D_0), average corrected cavity volume (V_0), and cavity number density in 87R DPT W irradiated at 973 K.

Material / Irradiation	Depth (nm)	Under-focus (μm)	Cavity Number n	Ring D_{in} (nm)	Corr. Factor (D_{in}^i)	Corr. D_0 (nm)	Corr. V_0 (nm^3)	Foil Thickness (nm)	Number Density (1/cm^3)
W / Ni^+ & He^+	100	-0.7685	422	1.6	0.88	1.9	3.4	51.5	1.0×10^{18}
NiFeW / Ni^+ & He^+	190	-0.7685	54	8.0	0.88	9.1	466	58.7	9.8×10^{15}
Boundary / Ni^+ & He^+	160	-1.5	30	4.6	0.81	5.6	95.2	56.4	2.2×10^{17}
W / He^+	50	-0.5	187	2.1	0.87, 0.89	2.4	7.2		
NiFeW / He^+	270	-0.5	53	9.0	0.91	9.9	533		
Boundary / He^+	290	-0.5	20	5.6	0.87, 0.88, 0.91	6.3	146		

Note: Both D_{in} and D_0 are subject to an uncertainty of ±0.2 nm in W or NiFeW and ±0.5 nm at boundaries.
Cavity number density at the interphase boundary is estimated based on boundary thickness of $2D_0$.
Cavity number density is subject to an uncertainty of up to ~10% or larger.

where D_{in}^i is the ring diameter of the ith cavity and n is the total number of the cavities under analysis. From Equation (1), the average diameter D_{in} of the measured cavities is 1.6 nm for $n = 422$, as listed in

Table 3. However, the measured cavity diameter D_{in}^{i} can be affected by defocus conditions and a number of other factors, including the D_{in}^{i} value and electron accelerating voltage. Based on a previous multi-slice simulation [23], the actual diameter D_0^i of the *i*th cavity can be obtained from

$$D_0^i = D_{in}^i / f\left(D_{in}^i\right), \tag{2}$$

where $f\left(D_{in}^i\right)$ is a correction factor. Under the imaging conditions, including defocus value of -0.7685 μm, illumination semi-angle of 0.3 mrad and accelerating voltage of 200 kV, the correction factor for D_{in}^i values smaller than 2.5 nm, $f\left(D_{in}^i\right)$ can be taken as 0.88 based on the reported data [23]. The corrected cavity diameter distribution D_0^i is shown in Fig. 8(b). The average corrected cavity diameter D_0 can be calculated from [22]

$$D_0 = \frac{1}{n}\sum_{i=1}^{n} D_0^i = \frac{1}{n}\sum_{i=1}^{n} D_{in}^i / f\left(D_{in}^i\right). \tag{3}$$

From Equation (3), the average corrected cavity diameter D_0 in is 1.9 nm, as indicated in Fig. 4 and listed in Table 3. Similarly, the volume V_0^i of the *i*th cavity, which is proportional to the number of He atoms inside the cavity, is estimated assuming that the cavity is a sphere with a diameter of D_0^i. The average corrected cavity volume V_0 is

$$V_0 = \frac{1}{n}\sum_{i=1}^{n} V_0^i = \frac{1}{n}\sum_{i=1}^{n} (\pi/6)\left(D_{in}^i / f\left(D_{in}^i\right)\right)^3. \tag{4}$$

The corrected cavity volume distribution V_0^i is also shown in Fig. 8(b) with an average corrected volume of 3.4 nm^3 obtained from Equation (4). In Fig. 8(a), the total number *n* of the identified and measured cavities is 422 over an area of 90 nm × 90 nm. The foil thickness at the image center was determined by EELS to be 51.5 ± 4.2 nm, as given in Table 3. Therefore, the cavity number density is deduced to be 1.0×10^{18} cavities/cm^3. The data accuracy could be affected by possible missing counts, cavity image overlapping over the foil thickness, and the uncertainty of the foil thickness (thickness uniformity and measurement error on the order of several nanometers), as reported previously [22]. The measurement uncertainty for cavity diameters is ~0.2 nm in W and NiFeW and ~0.5 nm along the interphase boundaries in this study. Cavity number density is accurate to ~10% or larger.

Fig. 9(a) shows the microstructure of NiFeW in the same sample as for Fig. 8. The corrected diameter distribution is shown in Fig. 9(b) with the average corrected cavity diameter of 9.1 nm, as compared to 1.9 nm in W [Fig. 8(b)], representing an increase by about a factor of 5. In addition to the general factors affecting the cavity growth rate discussed above, dose-rate effects on the cavity size [22] in this study could also play a role. The rastering ion beams used for irradiation could contribute to the dose-rate effects, as have been observed in pure Fe [24]. The average corrected volume of the cavities in Fig. 9(a) is estimated to be 466 nm^3. The total cavity count is 54 within the imaging field of view 307 nm × 307 nm. Based on the foil thickness of 58.7 ± 1.7 nm determined by EELS at the image center (depth = 190 nm), the cavity number density is estimated to be 9.8×10^{15} cavities/cm^3, as listed in Table 3. This density is ~2 orders of magnitude lower than that in W. Large faceted cavities (up to 15.4 nm) in the NiFeW phase are observed in Fig. 9(a). Quick K-P SRIM simulations suggest that the average number of vacancies

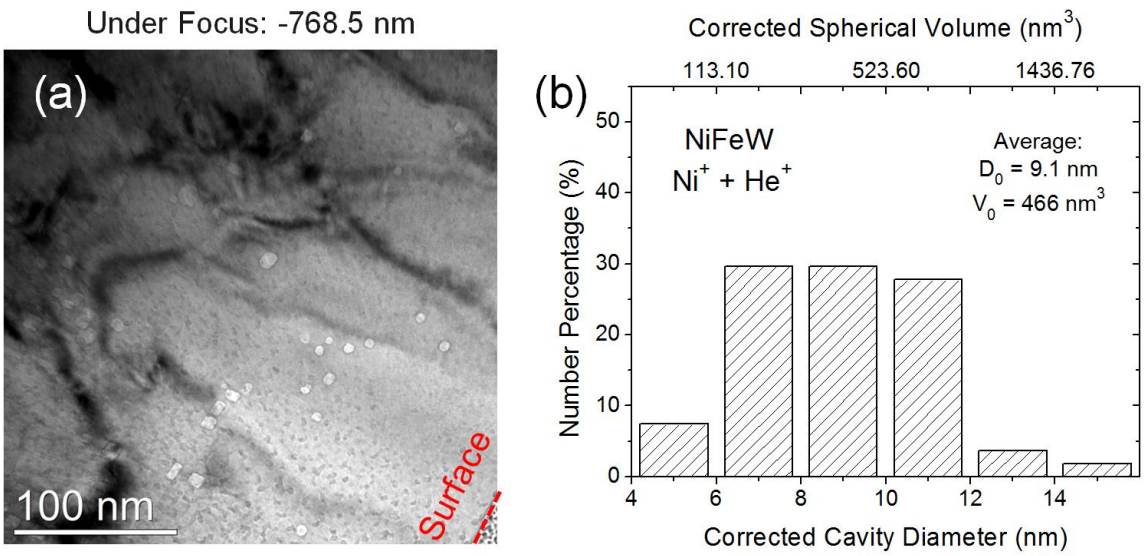

Figure 9. (a) TEM image showing a spatial distribution of He cavities at the image center depth of ~190 nm in the NiFeW phase within an 87R DPT W sample irradiated sequentially to 2.15×10^{16} Ni^+/cm^2 and 6.5×10^{15} He^+/cm^2 at 973 K. (b) Corrected He cavity diameter and volume distributions.

produced by each 90 keV He^+ ion in NiFeW and W in this study is 51 and 15 vacancies/ion, respectively. He atoms are expected to interact with the mobile mono-vacancies, resulting in the formation of He-vacancy clusters or He cavities [25-27] during irradiation, similar to the case of those in Fe [28,29]. The excessive number of vacancies could lead to formation of faceted cavities with inclusion of He atoms at a low gas pressure. It should be pointed out that SRIM simulations also suggest that thousands of vacancies per ion were produced by pre-irradiation with 1.2 MeV Ni^+ ions in NiFeW and W. However, these mobile mono-vacancies could interact with each other and form immobile vacancy clusters or disappear at boundaries or surfaces during irradiation at 973 K, as further discussed below.

Fig. 10 shows a preferential distribution of cavities along the W/NiFeW interphase boundary. These cavities have an average corrected diameter D_0 of 5.6 nm and an average corrected volume of 95.2 nm^3, which are between their corresponding values in NiFeW and W. If we take $2D_0$ as the boundary thickness, the cavity number density on the boundary (length = 218 nm and foil thickness = 56.4 ± 2.0 nm) is deduced to be 2.2×10^{17} cavities/cm^3, which is also between the corresponding values in NiFeW and W. Within the boundary thickness, the areal density corresponds to 2.4×10^{11} cavities/cm^2. While no interfacial cracking was observed during irradiation, aggregation of dense cavities at the interphase boundary could weaken the interfacial cohesion, which can shorten the lifetime of the material in service if used in fusion energy systems. Further studies are needed to address this issue.

In addition, STEM-EDS mapping was performed to study any Ni precipitation in W during Ni^+ ion irradiation. The results are shown in Fig. 11 for both Ni and W maps over the same area as in Fig. 10(a). The Ni and W maps do not show any fine features and there is no evidence for Ni particle precipitation in W. SRIM13 simulation predicts a maximum Ni concentration of 0.98 at.% in W at the depth of 294 nm [Fig. 1(a)] without taking thermal diffusion into account, compared to the Ni solubility limit of 0.1 wt.% or 0.36 at.% in W at 973 K [30].

Fig. 12 shows the cavity distribution near a W/W grain boundary at the image center depth of ~200 nm from the surface. In contrast to the interphase boundary in Fig. 10(a), there is no preferential

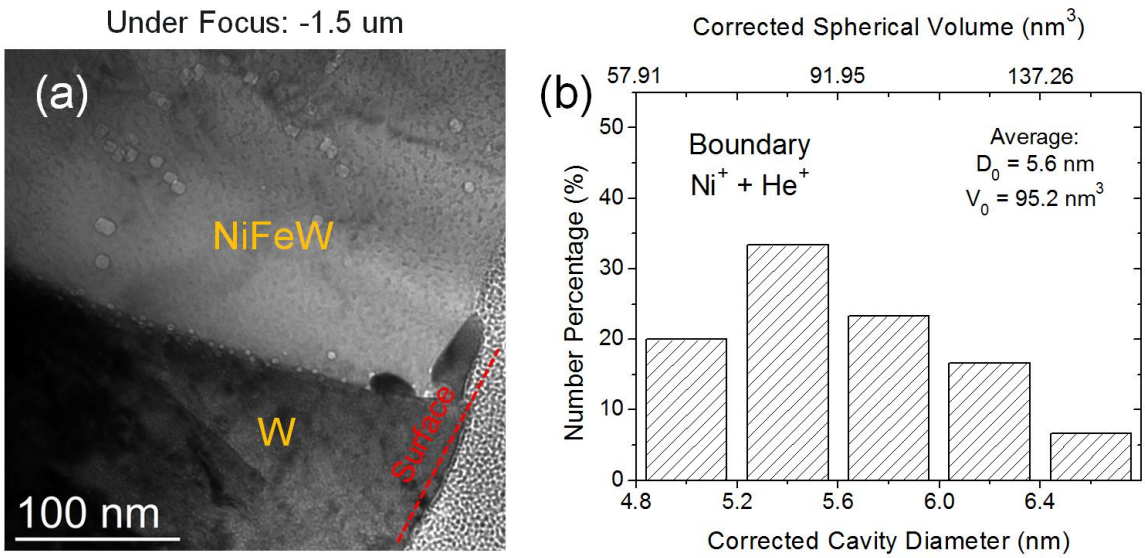

Figure 10. (a) TEM image showing a spatial He cavity distribution along an interphase boundary in an 87R DPT W sample irradiated sequentially to 2.15×10^{16} Ni^{+}/cm^{2} and 6.5×10^{15} He^{+}/cm^{2} at 973 K. (b) Corrected He cavity diameter and volume distributions.

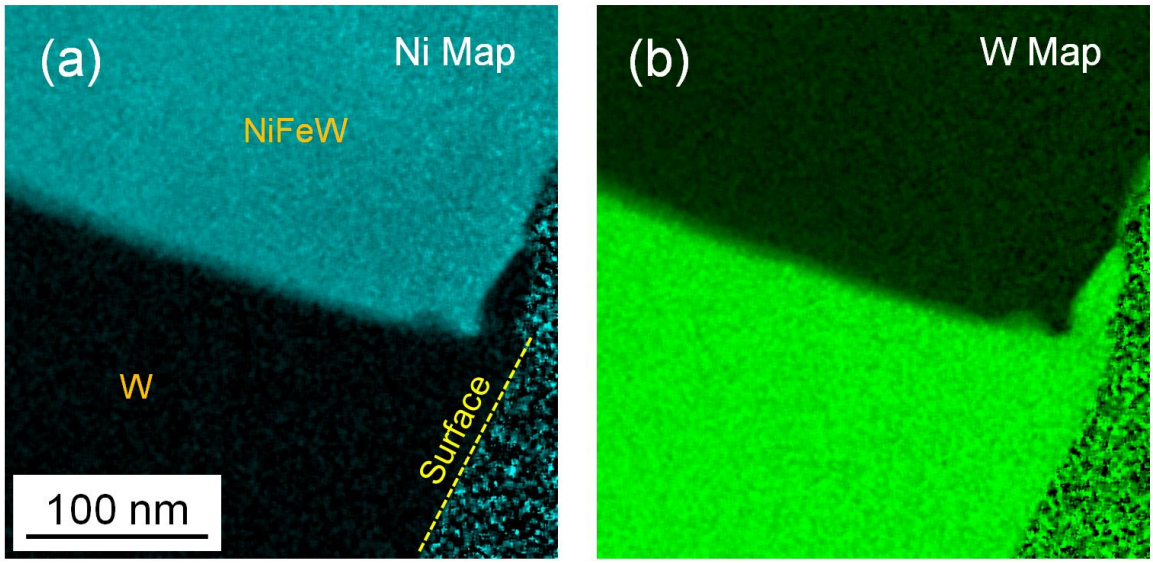

Figure 11. STEM-EDS maps of (a) Ni and (b) W in an 87R DPT W sample irradiated sequentially to 2.15×10^{16} Ni^{+}/cm^{2} and 6.5×10^{15} He^{+}/cm^{2} at 973 K.

distribution of cavities along the W/W grain boundary. Instead, cavities are distributed uniformly across the boundary. El-Atwani *et al*. [31] observed a uniform distribution of He bubbles near the grain boundaries in both ultrafine-grained and nano-grained W irradiated with He^{+} ions to 1.5×10^{18} He^{+}/cm^{2} at room temperature. However, the same study shows that He bubbles decorating grain boundaries were formed in the materials irradiated to 3.6×10^{15} He^{+}/cm^{2} and higher at 1223 K. Further investigations are planned for the cavity formation and related effects in 87R DPT W as a function of irradiation temperature and the results will be reported at a later date.

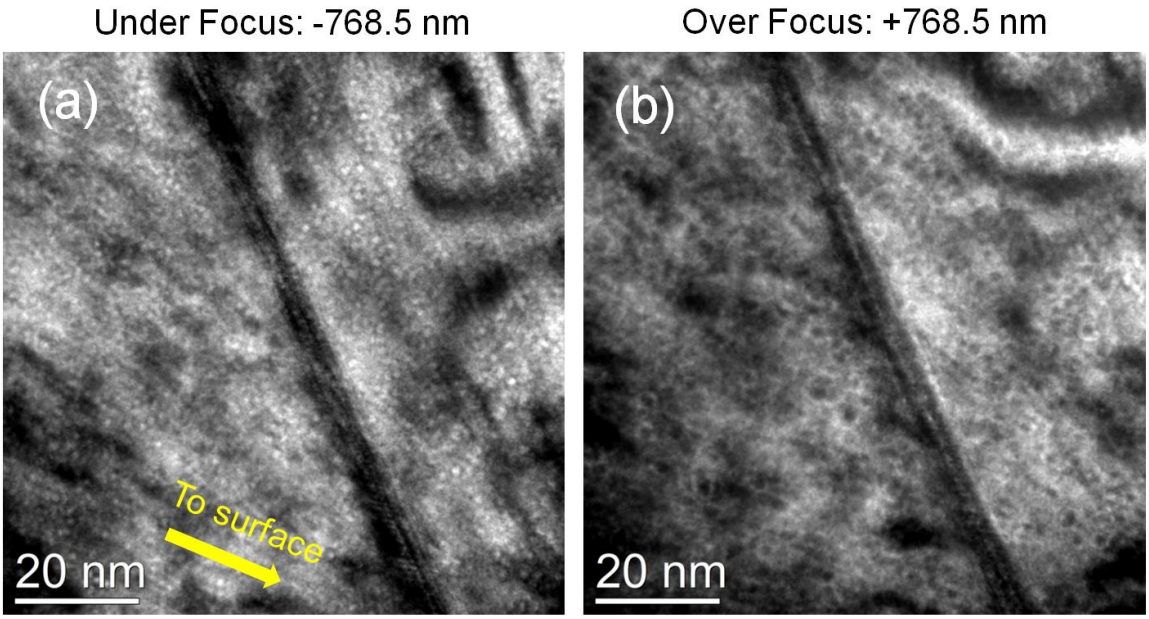

Figure 12. TEM images showing a spatial distribution of He cavities at the image center depth of ~200 nm with a W/W grain boundary in an 87R DPT W sample irradiated sequentially to 2.15×10^{16} Ni^+/cm^2 and 6.5×10^{15} He^+/cm^2 at 973 K: (a) under focus and (b) over focus.

3.3. Microstructure in 87R DPT W irradiated with Ni^+ ions

A previous study [31] indicated that vacancy generation and migration are needed to enhance trapping of He at W grain boundaries. Vacancies can enhance bubble growth by increasing the He mobility through the W matrix in the form of He-vacancy complexes. Once in the boundaries, both the He and vacancies can migrate and agglomerate to form bubbles. In order to study the mechanisms responsible for the preferential formation of He cavities along the interphase boundaries in 87R DPT W, additional microscopy studies of two regions irradiated with only Ni^+ and only He^+ ions have also been performed. Fig. 13 shows the under- and over-focus images of 87R DPT W near an interphase boundary irradiated with 1.2 MeV Ni^+ to a fluence of 2.15×10^{16} Ni^+/cm^2 at 973 K. The image center is located at the depth of ~200 nm. Fresnel aperture diffraction theory indicates that small cavity-type defects should show central bright and dark spots with under- and over-focus imaging, respectively. These features are not apparent in the Ni^+ ion irradiated W region shown in Fig. 13, in a sharp contrast to a high density of small voids observed in polycrystalline W irradiated with self-ions to only 1 dpa at 900 K [22]. Possible reasons include a significant simultaneous recovery of point defects produced in DPT W during Ni^+ ion irradiation at 973 K. It is known that lighter-ion irradiation produces a lower density of point defects within a single damage cascade, leading to a lower probability for formation of larger, more stable defect complexes during the defect relaxation process. Small defect clusters (~1 nm in size or smaller), if present, could not be visualized by TEM in this study. Also from Fig. 13, there are bright and dark lines along the boundary in the under-focus and over-focus images, respectively, as encapsulated in yellow. It is premature to claim its identity at this time, and further studies are needed to determine if the feature is associated with a misfit dislocation, a vacancy platelet that might form as a result of vacancy diffusion and clustering at the boundary, or simply an artifact. Fig. 13 also shows dark spots in the under-focus image and the corresponding bright spots in the over-focus image in the NiFeW phase, as encircled in red.

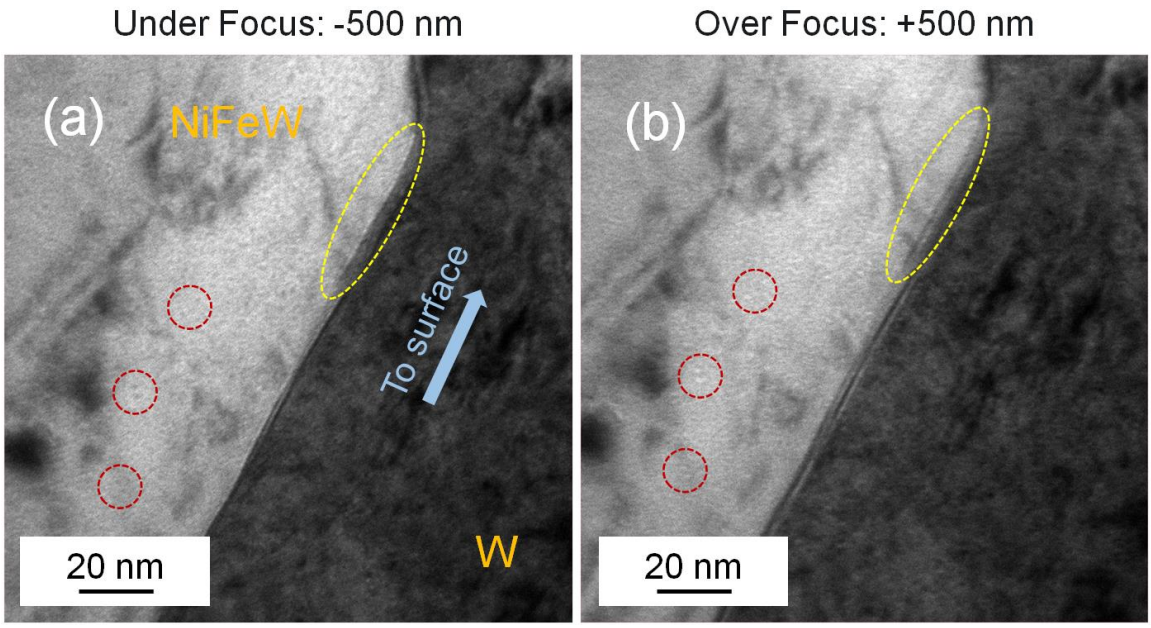

Figure 13. TEM images of microstructure at the image center depth of ~200 nm with a W/NiFeW interphase boundary in an 87R DPT W sample irradiated to 2.15×10^{16} Ni^{+}/cm^{2} at 973 K: (a) under focus and (b) over focus.

These features show a reverse Fresnel diffraction effect, which is not related to cavity types of defects. Their identities are also unknown and further investigations are needed for clarification.

In addition, the composition in W after Ni^{+} ion irradiation was also characterized using STEM-EDS mapping. The data (not shown) are similar to Fig. 11. Again, there is no evidence for Ni particle precipitation in W. Quick K-P SRIM simulations suggest that the average vacancy production rates in W and NiFeW irradiated with 1.2 MeV Ni^{+} ions in this study correspond to 2,625 and 4,998 vacancies/ion. In the absence of He atoms, some of these mobile mono-vacancies could be annihilated by combining with self-interstitial atoms or could disappear by migrating to grain boundaries or surfaces. Other mono-vacancies could interact with each other and form small immobile vacancy clusters that are too small to be visualized by TEM. Survival of mono-vacancies is unlikely in both W and NiFeW after irradiation.

In order to ensure Ni^{+} ion irradiation was done as intended, STEM-EDS mapping with inclusion of an interphase boundary was performed in several locations for an extended time to improve data statistics. Fig. 14(a) shows the probing area with vertical and horizontal line scans indicated by yellow arrows in an STEM image. The bright contrast with a darker band (thicker region) on the left is the W phase. As noted above, the implanted Ni atomic concentration in W is predicted to show a peak concentration of 0.98 at.% at 294 nm according to SRIM simulation [Table 1 and Fig. 1(a)]. From Fig. 14(b), the vertical line scan from the surface to a deeper region (~1.2 μm in depth) at a location far away from the W/NiFeW boundary shows that there is a Ni concentration peak (~1 at.%) in W at the depth of ~300 nm, which is consistent with the SRIM simulation. The implanted Ni atoms tend to diffuse inward and outward, and some Ni atoms appear to accumulate at the surface. Fig. 14(c) shows the Ni and Fe concentrations across the interphase from three horizontal line scans with the profiles shifted to align them with the boundary. From Fig. 14(c), Ni concentration profiles from the horizontal line scans at the middle and bottom locations appear to be the same within the statistical fluctuation. This is an expected result because both of the locations are well beyond the Ni^{+} ion projected range. The horizontal line scan in the top location that includes the implanted Ni region shows a statistically higher Ni concentration than the middle and

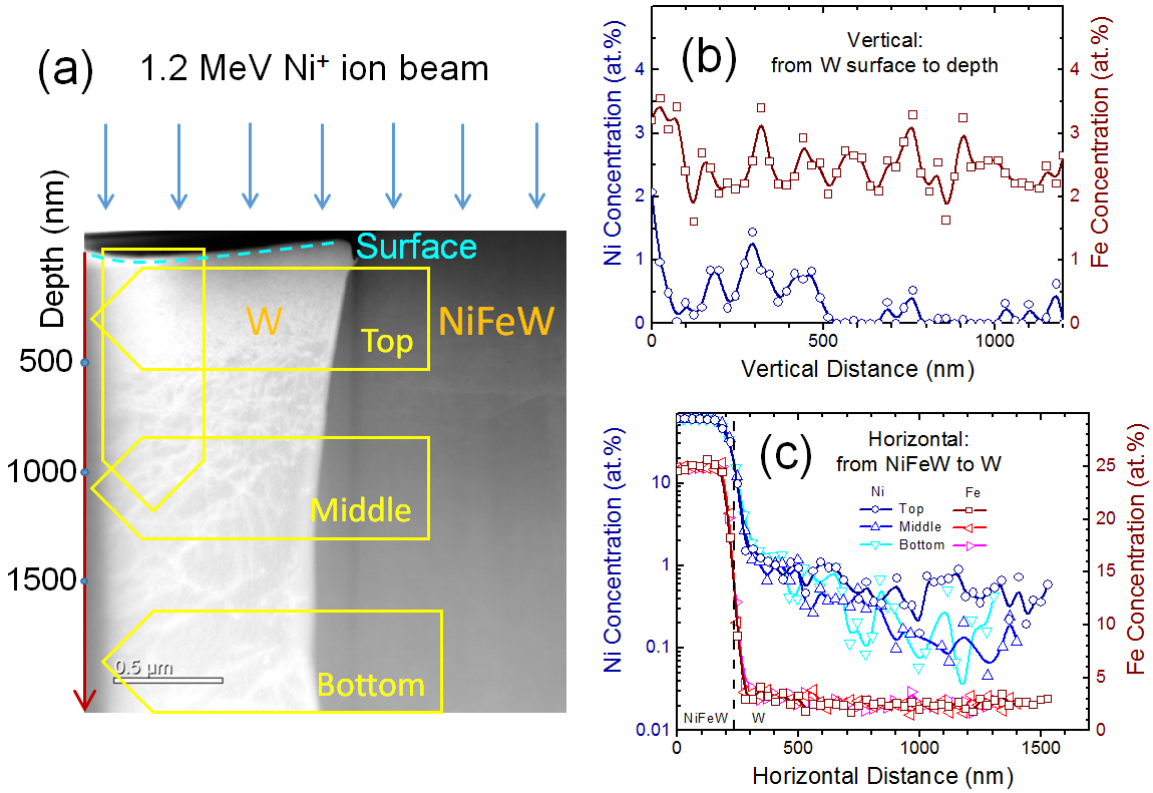

Figure 14. (a) STEM-EDS line scans for the depth profiles of Ni and Fe concentrations in the W phase within an 87R DPT W sample irradiated to 2.15×10^{16} Ni^{+}/cm^{2} at 973 K, (b) Ni and Fe profiles from a vertical scan, and (c) Ni and Fe profiles from three horizontal scans (profiles shifted to align with the boundary).

bottom line scans at the distance larger than 700 nm from the boundary, confirming the presence of the implanted Ni atoms in the near-surface region. Also from Figs. 14(b) and (c), there appears to be a small Ni concentration of ~0.1 at.% well beyond the Ni^{+} ion projected range in the W phase. The Fe concentration shows a fairly flat profile at a level of ~2.5 at.% in W. Thus, the W grain has a purity of ~97.4 at.% or ~99.2 wt.%, which is largely consistent with 99.5 wt.% from a previous report [9] for W grains within DPT W prior to hot-rolling (0R DPT W).

3.4. Helium cavities in 87R DPT W irradiated with He^{+} ions

In contrast to Ni^{+} ion irradiation, He cavities are observed in W irradiated with He^{+} ions only, as shown in the framed area of Fig. 15(a), where a spatial distribution of the cavities in the near the surface region is imaged with conventional TEM under a defocused (-500 nm) condition. The corrected diameter and volume distributions of the He cavities are shown in Fig. 15(b), where the average corrected cavity diameter is 2.4 nm and the average corrected volume is 7.2 nm^{3} as indicated in the figure and given in Table 3. The FIB sample irradiated with He^{+} ions only dropped from the grid after TEM. Further STEM-EELS for the sample could not be followed and He cavity density in the sample could not be determined. This is unfortunate, but this study focuses on the DPT W irradiated with both Ni^{+} and He^{+} ions for emulation of fusion irradiation conditions.

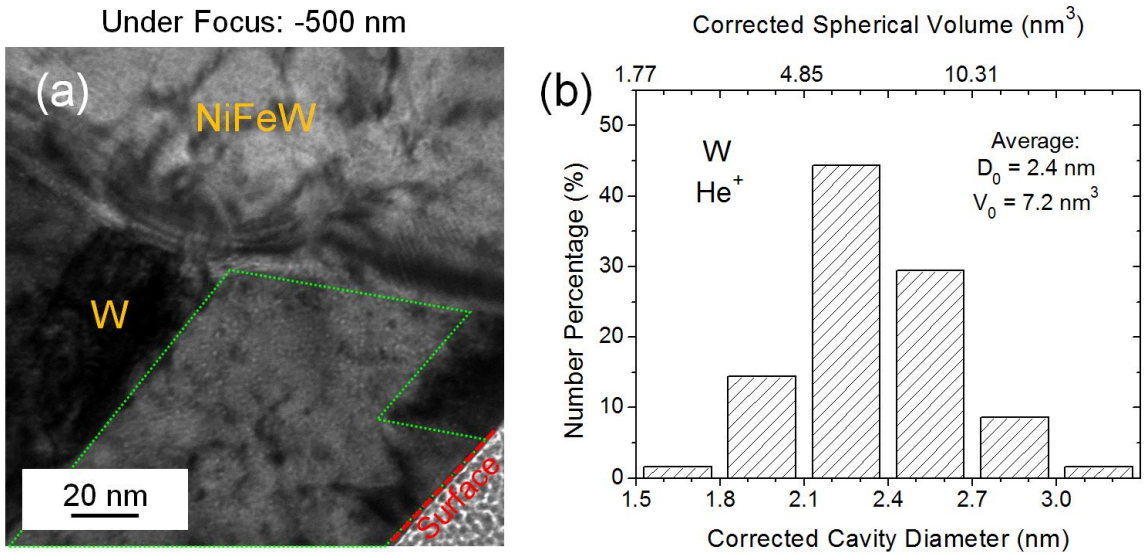

Figure 15. (a) TEM image showing a spatial distribution of He cavities around the depth of ~50 nm in the framed W phase within an 87R DPT W sample irradiated to 6.5×10^{15} He^+/cm^2 at 973 K. (b) Corrected He cavity diameter and volume distributions.

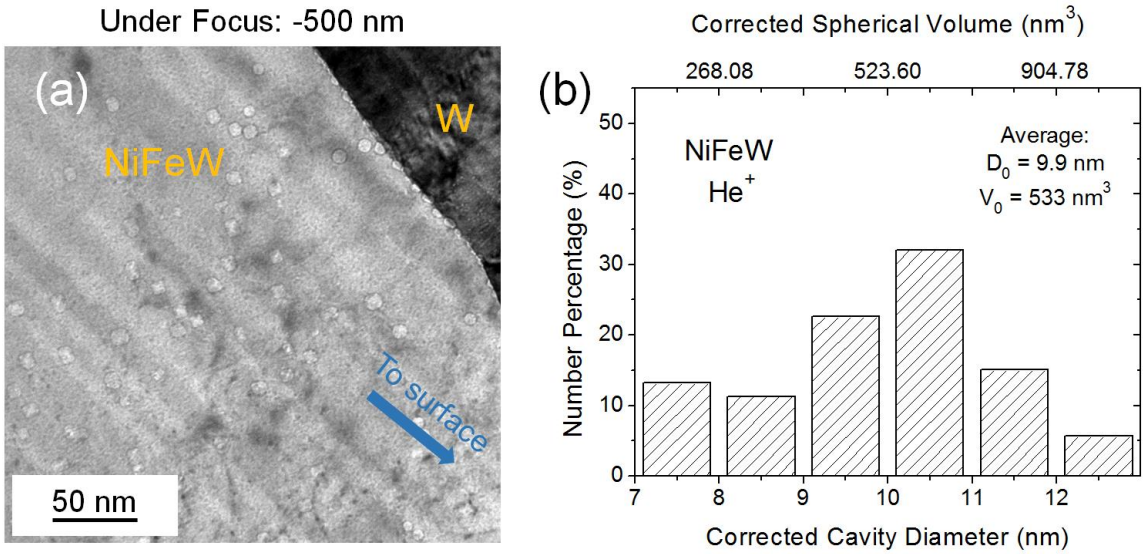

Figure 16. (a) TEM image showing a spatial distribution of He cavities at the image center depth of ~270 nm in the NiFeW phase within an 87R DPT W sample irradiated to 6.5×10^{15} He^+/cm^2 at 973 K. (b) Corrected He cavity diameter and volume distributions.

Fig. 16 shows the microstructure of NiFeW after He^+ ion irradiation. Apparently, the cavities in NiFeW are much larger than in W, similar to the case of sequential ion irradiation. The average corrected cavity diameter is 9.9 nm in NiFeW. This value is more than 4 times larger than that (2.4) nm in W (Fig. 15), but only slightly larger than that (9.1 nm) in NiFeW for the case of sequential irradiation. There is also a preferential distribution of cavities along the interphase boundary under irradiation with He^+ ions only, as shown in Fig. 17. These cavities have an average corrected diameter of 6.3 nm with an average corrected volume of 146 nm^3.

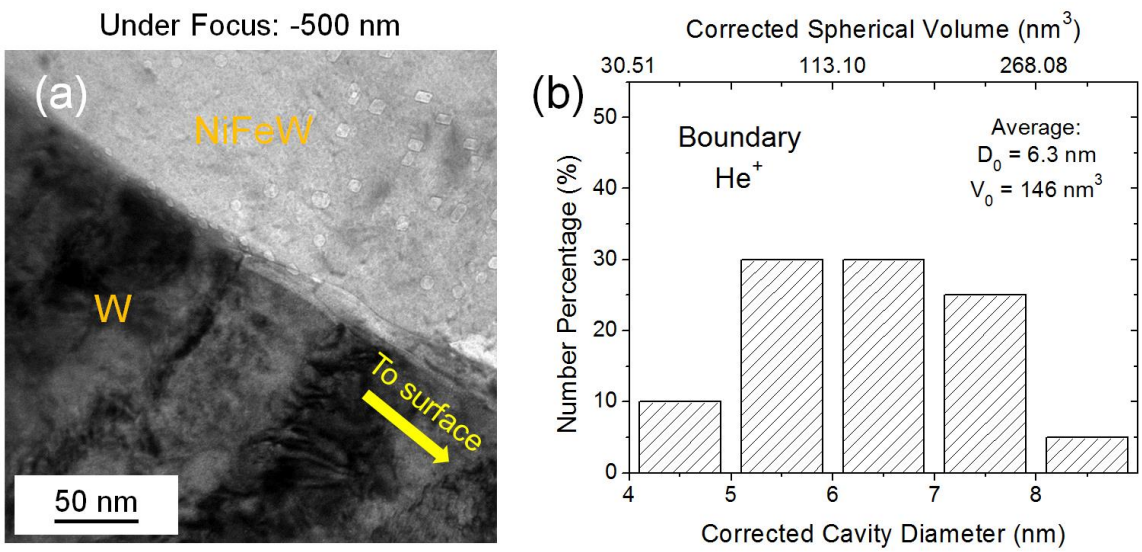

Figure 17. (a) TEM image showing a spatial distribution of He cavities at the image center depth of ~290 nm along an interphase boundary in an 87R DPT W sample irradiated to 6.5×10^{15} He^+/cm^2 at 973 K. (b) Corrected He cavity diameter and volume distributions.

In all the cases above, the average corrected cavity diameter or volume appears to be larger in the He^+ ion irradiated sample than that the sequentially irradiated sample. Significant simultaneous processes involving defect recovery and clustering in 87R DPT W are expected during Ni^+ ion irradiation at 973 K. As discussed above, survival of mono-vacancies is unlikely in both W and NiFeW after Ni^+ ion irradiation. The resulting microstructure could contain small defect clusters that are not visible to TEM. These immobile defect clusters could serve as centers to trap some of the migrating vacancies and He atoms to form visible He cavities in W and NiFeW during He^+ ion irradiation at 973 K. This type of microstructure could have a preference of growth over nucleation of He cavities, leading to a larger number density of smaller cavity sizes compared to a microstructure without pre-existing defects. Dual-beam irradiation might be a better approach to emulate high-energy neutron irradiation because more mono-vacancies would be available during He^+ ion irradiation, which could interact with He atoms or He-vacancy defect complexes to potentially form larger He cavities and/or higher number densities.

4. Conclusions

An 87R DPT W composite with brittle W phase particles embedded in a ductile NiFeW phase matrix was irradiated sequentially with Ni^+ and He^+ ions at 973 K to emulate a microstructure. Both the doses (27 dpa in W and 31 dpa in NiFeW) and He concentrations (0.48 at.% in W and 0.39 at.% in NiFeW) in the composite are comparable to those after 5-year irradiation in a conceptual fusion power plant. A lower number density (9.8×10^{15} cavities/cm^3) of larger He cavities (9.1 nm in diameter) in NiFeW than W (1.0×10^{18} cavities/cm^3 and 1.9 nm in diameter) is observed. There is a preferential distribution of medium-sized He cavities (5.6 nm in diameter) along the W/NiFeW interphase boundary. In contrast, He cavities are distributed uniformly across the W/W grain boundaries under the same irradiation conditions. Large faceted cavities (up to 15.4 nm) in the NiFeW phase and a relatively uniform cavity distribution in the near-surface region of the W phase are observed. Pre-irradiation with Ni^+ ions at 973 K does not provide any evidence for formation of visible voids or Ni precipitates in W. However, it could create

immobile defect clusters that are not visible to TEM. These defect clusters could serve as centers to trap some of the migrating vacancies and He atoms to form visible He cavities in W and NiFeW during He^+ ion irradiation at 973 K. This process could lead to a larger number density of smaller cavity sizes, as observed by this study that shows the average corrected cavity diameter or volume is slightly larger in the He^+ ion irradiated sample than sequentially irradiated sample. Formation of the He cavities is a result of either interaction between migrating vacancies and He atoms or trapping by existing defects in W and NiFeW during He^+ irradiation at 973 K. As significant simultaneous processes involving defect recovery and clustering in 87R DPT W during Ni^+ ion irradiation at 973 K are expected, dual-beam irradiation with Ni^+ and He^+ ions might be able to better emulate high-energy neutron irradiation in DPT W at elevated temperatures, where more mobile vacancies are available to interact with He atoms or He-vacancy defect clusters to potentially form larger He cavities and/or higher number densities.

Acknowledgements

This research was supported by Office of Fusion Energy Sciences, U.S. Department of Energy (DOE) and performed at the Pacific Northwest National Laboratory under Contract DE-AC05-76RL01830. A portion of the research was performed using EMSL, a DOE Office of Science User Facility sponsored by the Biological and Environmental Research program. The authors are grateful to Charles Henager for providing 87R DPT W sample for this study and to Bethany Mathews and Alan Schemer-Kohrn for FIB sample preparation.

References

[1] R.A. Causey, T. J. Venhaus, Phys. Scr. T94 (2001) 9.
[2] E. Lassner, W.S. Schubert, Tungsten: Properties, Chemistry, Technology of the Element, Alloys and Chemical Compounds, Springer, New York, NY, 1999. P.30.
[3] D.M. Duffy, Phil. Trans. R. Soc. A 368 (2010) 3315.
[4] M. Rieth, S.L. Dudarev, S.M. Gonzalez de Vicente, J. Aktaa, T. Ahlgren, S. Antusch *et al*., J. Nucl. Mater. 432 (2013) 482.
[5] R.G. Abernethy, Mater. Sci. Technol. 33 (2017) 388.
[6] S.J. Zinkle, J.T. Busby, Mater. Today 12 (2009) 12.
[7] H. Ullmaier, F. Carsughi, Nucl. Instrum. Methods Phys. Res. B. 101 (1995) 406.
[8] M. Rieth , J.L. Boutard, S.L. Dudarev, T. Ahlgren, S. Antusch, N. Baluc *et al*., J. Nucl. Mater. 417 (2011) 463.
[9] C.H. Henager, Jr., W. Setyawan, T.J. Roosendaal, N.R. Overman, B.A. Borlaug, E.L. Stevens *et al*., Int. J. Powder Metall. 53 (2017) 53.
[10] R. Neu , H. Maier , M. Balden , R. Dux , S. Elgeti , H. Gietl *et al*., J. Nucl. Mater. 511 (2018) 567.
[11] M.E. Alam , G.R. Odette , Acta Mater. 186 (2020) 324.
[12] J.V. Haag IV, D.J. Edwards, C.H. Henager Jr., W. Setyawan, J. Wang, M. Murayama, Acta Mater. 204 (2021) 116523.
[13] https://www.mttm.com/tungsten-alloys.
[14] A. Pathak, A. Panchal, T.K. Nandy, A.K. Singh, Int. J. Refract. Met. Hard Mater. 75 (2018) 43.
[15] M.R. Gilbert, J.-Ch. Sublet, Nucl. Fusion 51 (2011) 043005.
[16] Fusion Evaluated Nuclear Data Library Ver.3.1d (FENDL-3.1d) at https://www-nds.iaea.org/fendl/.

[17] M.R. Gilbert, S.L. Dudarev, S. Zheng, L.W. Packer, J.-Ch. Sublet, Nucl. Fusion 52 (2012) 083019.
[18] J.F. Ziegler, J.P. Biearsack, U. Littmark, *The stopping and Range of Ions in Solids* (Pergamon Press, New York, 1985); available at: http://www.SRIM.org/.
[19] ASTM, ASTM Standard E521-96 (2009), *Standard Practice for Neutron Radiation Damage Simulation by Charged-Particle Irradiation*, ASTM International, West Conshohocken, PA (2009).
[20] R.E. Stoller, M.B. Toloczko, G.S. Was, A.G. Certain, S. Dwaraknath, F.A. Garner, Nucl. Inst. Meth. Phys. Res. B. 310 (2013) 75.
[21] S. Agarwal, Y. Lin, C. Li, R.E. Stoller, S.J. Zinkle, Nucl. Inst. Meth. Phys. Res. B. 503 (2021) 11.
[22] W. Jiang, Y. Zhu, L.M. Zhang, D. J. Edwards, N. R. Overman, G. Nandipati, *et al*., J. Nucl. Mater. 550 (2021) 152905.
[23] B. Yao, D.E. Edwards, R.J. Kurtz, G.R. Odette, T. Yamamoto, J. Electron Microsc. 61 (2012) 393.
[24] J.G. Gigax, E. Aydogan, T. Chen, D. Chen, L. Shao, J. Nucl. Mater. 465 (2015) 343.
[25] N. Yoshida, J. Nucl. Mater. **266** (1999) 197.
[26] C.S. Becquart, C. Domain, J. Nucl. Mater. 386-388 (2009) 109.
[27] F. Hofmann, D. Nguyen-Manh, M.R. Gibert, C.E. Beck, J.K. Eliason, A.A. Maznev, *et al*., Acta Mater. 89 (2015) 352.
[28] K. Morishita, R. Sugano, B.D. Wirth, T.D. de la Rubia, Nucl. Instr. Meth. B 202 (2003) 76.
[29] C.-C. Fu, F. Willaime, Phys. Rev. B 72 (2005) 064117.
[30] H. Okamoto, M.E. Schlesinger, E.M. Mueller, editors, *ASM Handbook Volume 3: Alloy Phase Diagrams*, ASM International, West Conshohocken, PA (2016), p. 531; DOI: 10.31399/asm.hb.v03.a0006162.
[31] O. El-Atwani, J.A. Hinks, G. Greaves, S.S. Harilal, A. Hassanein, J. Nucl. Mater. 458 (2015) 216.